

Thermal Decoherence and Population Transfer of MeV Channeling Electrons in Diamond

Tadas Paulauskas

Center for Physical Sciences and Technology, Saulėtekio al 3, Vilnius LT-10257,
Lithuania

Abstract

Channeling radiation in oriented crystals arises from transitions between quantized transverse bound states in the MeV regime and is strongly affected by thermal diffuse scattering through population transfer and decoherence. A frozen-phonon multislice propagation framework is developed to track a reduced transverse Hilbert space spanned by selected bound-state manifolds using configuration-resolved projection amplitudes. Beyond reproducing transition energies, the method yields reduced manifold density matrices, thermal population kinetics, and depth-resolved coherence metrics. Applied to axial electron channeling in $\langle 100 \rangle$ diamond at 16.9 MeV, the results show approximately exponential population loss with strongly state-dependent feeding among low-lying manifolds. For an initial coherent superposition in the degenerate $2p$ manifold, the intra-manifold purity relaxes toward the maximally mixed limit, consistent with thermally induced random basis rotations. Under $1s$ initial excitation, population transferred into the $2p$ and $3d$ manifolds remains close to maximally mixed, while weak cross-manifold coherences persist. The framework enables quantitative analysis of thermal population dynamics, decoherence, and their links to spontaneous and coherently driven emission observables across a broad range of crystal structures.

Keywords: channeling radiation, axial channeling, frozen-phonon multislice, thermal diffuse scattering, decoherence

I. INTRODUCTION

Charged particle channeling in oriented single crystals offers a paradigmatic system for studying motion in strong, periodic potentials. For electrons and positrons from the few-MeV to GeV range, the transverse dynamics can be quasi-bound to atomic columns (axial channeling) or planes (planar channeling) [1-3]. Transitions between quantized transverse states generate channeling radiation in the X-ray to γ -range, yet experimental spectral features are significantly affected by the coupling to the crystal lattice [4-7].

Classical trajectory descriptions are typically adequate at hundreds-MeV to GeV energies, where the density of bound transverse states becomes effectively quasi-continuous [8-9]. In the lower MeV regime, the transverse motion is strongly quantized, so quantum formulations are required to reproduce discrete transition lines. Standard theoretical approaches typically incorporate finite temperature effects via a static mean-field (Debye-Waller broadened) atomic potentials [6,8-13]. While this correctly shifts eigenenergies, it does not capture dynamical thermal diffuse scattering (TDS) effects, such as population transfer between bound states and the associated decoherence. Numerical quantification of coherence dynamics in axial channeling has remained limited, yet coherence can influence radiation observables, such as polarization and angular distributions, and is central to assessing external-field driven channeling-emission schemes [14-18].

A complementary route, adopted here, is to simulate the high-energy coherent wave propagation directly through crystal potential. In the paraxial approximation, the resulting Schrödinger-like evolution along the beam direction admits a split-operator factorization. The resulting multislice propagator naturally captures dynamical diffraction and channeling without additional coupling assumptions, and it generalizes to arbitrary crystal structures and lattice defects [19].

To include thermal effects beyond Debye-Waller smearing, the frozen-phonon (FP) method is employed [19-21]. FP reproduces TDS by sampling many static displaced lattices, propagating coherently for each configuration, and forming relevant observables via incoherent ensemble averages. In the channeling-radiation setting, this provides a microscopic description of TDS effects while retaining full wave mechanics.

In this article, a tracked transverse Hilbert space is defined in which selected bound-state manifolds are explicitly followed during FP multislice propagation. Depth-dependent manifold populations, reduced states within degenerate manifolds, and basis-invariant cross-manifold coherence measures are extracted from configuration-resolved projection amplitudes. The framework is applied to axial electron channeling in diamond in the 30-MeV-class regime, analyzing thermal population transfer and degenerate intra-manifold decoherence, as well as cross-manifold coherence for the radiative channels $2p \rightarrow 1s$ and $3d \rightarrow 2p$ under $1s$ -dominated excitation.

II. THEORY

A high-energy, spinless electron is treated within the standard relativistically corrected paraxial approximation. The wavefunction factors into a slowly varying transverse envelope $\psi(\mathbf{r}, z)$ multiplied by a high-momentum planewave, k_0 , along the optic axis z . Assuming constant total energy, z plays the role of the evolution parameter and the transverse envelope obeys Schrödinger-type equation:

$$(1) \quad \frac{i}{\sigma} \frac{\partial}{\partial z} \psi(\mathbf{r}, z) = \left[-\frac{\hbar^2}{2\gamma m_0} \nabla_{\mathbf{r}}^2 - V(\mathbf{r}, z) \right] \psi(\mathbf{r}, z),$$

where γ is relativistic factor and $\sigma = \gamma m_0 / k_0 \hbar^2$. The operator in brackets defines the transverse Hamiltonian $H_{\perp}(z)$. The formal solution is expressed via a z -ordered unitary propagator:

$$(2) \quad \psi(\mathbf{r}, z) = U(z, z_0) \psi(\mathbf{r}, z_0),$$

$$(3) \quad U(z, z_0) = \mathcal{T} \exp \left[-i \sigma \int_{z_0}^z H_{\perp}(z') dz' \right].$$

Numerically, the crystal is discretized into N slices of thickness Δz and a Suzuki–Trotter approximation is applied [22]. The slice potential is taken as the z -average over the slice:

$$(4) \quad V_j(\mathbf{r}) \approx \frac{1}{\Delta z} \int_{z_j}^{z_j + \Delta z} V(\mathbf{r}, z) dz.$$

Using the first-order (Lie–Trotter) split-operator, the per-slice propagator and wavefunction at thickness $N\Delta z$ are:

$$(5) \quad U_j = \exp[i\sigma K \Delta z] \exp[i\sigma V_j \Delta z],$$

$$(6) \quad \psi(\mathbf{r}, N \Delta z) = (\prod_{j=1}^N U_j) \psi(\mathbf{r}, 0).$$

The split-step is implemented efficiently using FFTs: the kinetic factor is diagonal in transverse reciprocal space, while the potential factor is diagonal in real space. Crystal is constructed from the Doyle–Turner (DT) parametrization of atomic potentials, commonly used in channeling radiation simulations [23]. The isotropic Debye–Waller (DW) factor with the two-dimensional mean square amplitude of thermal vibrations, u_{2d}^2 , is used to statically smear the DT atomic potential (numerical implementation described in Supplemental Materials).

Thermal diffuse scattering is treated here in the frozen-phonon approximation. The initial phonon state is a thermal distribution (statistical mixture), represented by p_n in diagonal basis $\{|\mu_n\rangle\}$, and an electron in a pure state $|\psi(0)\rangle$, giving initial density matrix:

$$(7) \quad \rho_{ph} \otimes \rho_e = \sum_n p_n |\mu_n\rangle \langle \mu_n| \otimes |\psi(0)\rangle \langle \psi(0)|.$$

In the FP approximation, the thermal phonon mixture is represented, under the harmonic approximation, by an ensemble of static lattice configurations indexed by β . For each configuration β , atomic positions are obtained by applying random thermal displacements $\mathbf{u}_l^{(\beta)}$ to each atom l , $\mathbf{R}_l^{(\beta)} = \mathbf{R}_l^{(0)} + \mathbf{u}_l^{(\beta)}$. The displacements $\mathbf{u}_l^{(\beta)}$ are sampled from a zero-mean Gaussian distribution with variance set by u_{2d}^2 . For a given configuration β the electron evolves under an effective electron-only propagator with static multislice potentials:

$$(8) \quad \psi^{(\beta)}(\mathbf{r}, z) = U^{(\beta)}(z, 0) \psi(\mathbf{r}, 0).$$

This contrasts with DW smearing, where the potential is analytically averaged and a single mean-field propagation is performed. In the FP approximation, experimentally relevant intensity-like observables and spectral densities are obtained by incoherent averaging, which is equivalent to tracing out the unobserved phonon subsystem ρ_{ph} .

The FP propagation does not by itself provide the transverse energies or modal content. Generally, the envelope $\psi(\mathbf{r}, z)$ admits an eigenmode expansion:

$$(9) \quad \psi(\mathbf{r}, z) \approx \sum_n c_n(z) \phi_n(\mathbf{r}) \exp[-i\sigma\varepsilon_n z], \quad c_n(0) = \int d^2 r \phi_n^*(\mathbf{r}) \psi(\mathbf{r}, 0).$$

To extract the localized (non-dispersive) bound states ϕ_n and their energies ε_n , a spectral method based on the z -propagation is used. Using Trotter propagation, the wavefunction autocorrelation $A(z)$ and its Fourier spectrum $S(k_z)$ are computed:

$$(10) \quad A(z) = \langle \psi(\mathbf{r}, 0) | \psi(\mathbf{r}, z) \rangle,$$

$$(11) \quad S(k_z) = \int_0^Z A(z) e^{ik_z z} dz.$$

Peaks in $|S(k_z)|$ occur at $k_{z,n} = \sigma\varepsilon_n$, enabling direct conversion between longitudinal spatial frequencies and transverse energies [12,13,24]. To extract an eigenmode associated with a chosen peak $k_{z,n}$, phase-compensated accumulation of the propagated wavefunction $\psi(\mathbf{r}, z_j)$ is performed over total M slices to pick out the desired eigenmode

$$(12) \quad \phi_n(\mathbf{r}) \approx \sum_{j=1}^M \psi(\mathbf{r}, z_j) e^{ik_{z,n} z_j} \Delta z.$$

Cross-correlation amplitudes and quantities derived from them are then computed to track manifold populations and coherence metrics with propagation depth.

III. RESULTS

A. Axial channeling radiation transition energies

Axial channeling radiation transition energies were first computed for diamond aligned to the $\langle 100 \rangle$ and $\langle 110 \rangle$ axes at several beam energies and compared against reported experimental values to validate the numerical approach [25,26]. Both thermal Debye–Waller smearing of the atomic potential (mean-field) and the frozen-phonon (FP) ensemble approach were used to compare the autocorrelation functions and the extracted transverse energy spectrum. The root mean square (RMS) two-dimensional thermal displacement amplitude, u_{2d} , for carbon is set to 0.055 Å and the same is used to parametrize the DW smearing. For $\langle 100 \rangle$ and $\langle 110 \rangle$ directions four and two equal-thickness slices per unit cell were used, respectively, corresponding to $\Delta z \approx 0.896$ Å and 1.426 Å.

To generate the autocorrelation function, the initial probe was chosen as a superposition of several transverse profiles with different symmetries and overlap onto the relevant deeply bound modes. Figure 1 shows the ensemble-averaged imaginary part of the FP autocorrelation, $Im\langle A^{(\beta)}(z) \rangle_\beta$, with $\beta = 10$ configurations for $\langle 100 \rangle$ diamond at 16.9 MeV and 30.5 MeV, together with the corresponding mean-field result.

In the FP case, the autocorrelation exhibits a clear decay with thickness, and the decay is stronger at 30.5 MeV. In contrast, no comparable decay is observed over the same thickness using DW-smeared potentials. This is consistent with stochastic transverse momentum transfer under thermal displacements, which is absent in a static mean-field description.

The transverse energy spectra are shown alongside the autocorrelations in Fig. 1. For the spectrum, absolute value of an incoherent ensemble average is used, $Abs\langle |S^{(\beta)}(k_z)| \rangle_\beta$. A central observation is that the extracted bound-state energies (peak positions) agree, up to the numerical energy-bin size ($E_{bin} \sim 0.5$ eV), between the FP and DW approaches. This agreement was observed across the tested beam energies for $\langle 100 \rangle$ and $\langle 110 \rangle$ orientations, indicating that the FP sampling reproduces the thermal diffuse effects at the level of eigen-energies. Peak widths are similar for both FP and DW cases and are set by decay rate of the bound-state as well as finite propagation depth, which imposes Fourier broadening and can dominate for weakly decaying states.

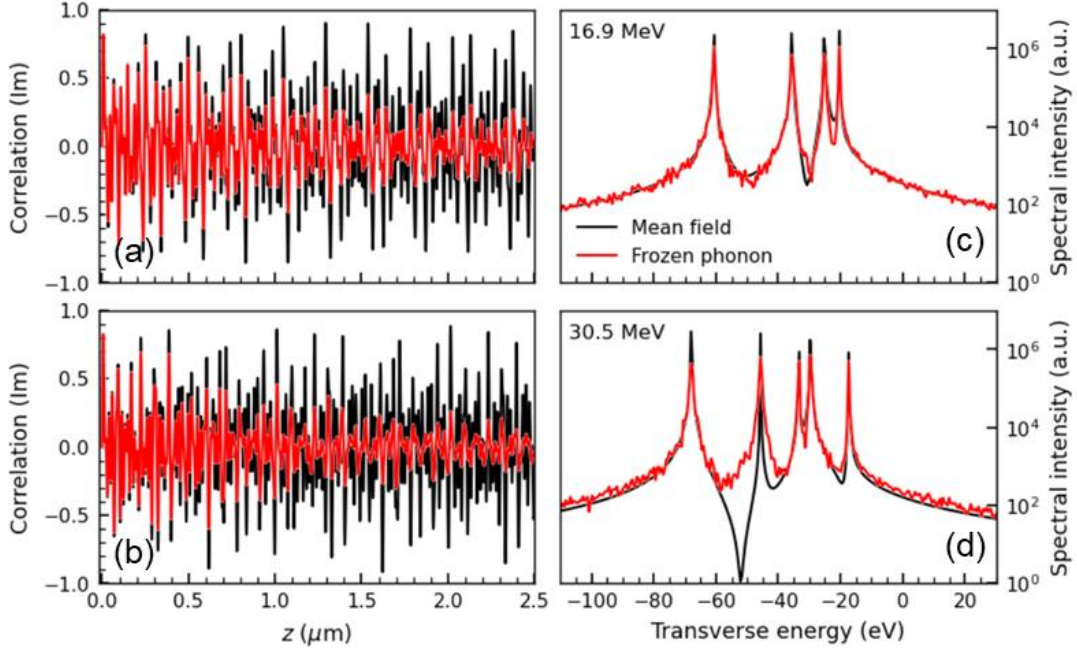


FIG. 1. (a, b) Imaginary parts of the ensemble-averaged autocorrelation functions at 16.9 MeV and 30.5 MeV beam energies. Mean-field (black) and frozen-phonon (red) calculations are overlaid. (c, d) Transverse energy spectrum plotted in its absolute value in log-scale.

The peaks in the transverse-energy spectrum in hydrogenic notation correspond to $1s$, $2p$, $2s$, $3d$, and $3p$ ($3p$ is excited here only in the 30.5 MeV case), from the deepest to shallower bound states, respectively. To relate the energy spacings ΔE of transitions to laboratory photon energies, the standard small-angle forward-emission approximation is used [1-3]:

$$(13) \quad E_\gamma(\theta) = \frac{2\gamma^2 \Delta E}{1 + \gamma^2 \theta^2}$$

Channeling radiation energies reported in Table 1 were evaluated at $\theta = 0$ and compared against experimentally quoted transition values for several beam energies and crystal orientations [25,26]. The agreement is generally highly satisfactory across most of the axial transitions, supporting the numerical implementation and the FP/DW consistency. The largest discrepancy is observed for the $3d \rightarrow 2p$ transition at 30.5 MeV, where the difference exceeds that of other transitions and may require closer scrutiny.

The transition energies are sensitive to the thermal displacement amplitude, particularly for the more deeply bound states. Values for u_{2d} in the range $0.050 - 0.070 \text{ \AA}$ are commonly

found in the literature when modelling thermal linewidth broadening, and the adopted value here (0.055 Å) provides a representative match to the measured transition energies [6,25].

Table 1. A comparison of experimentally reported and in this work calculated axial channeling radiation transition energies in diamond [25,26]. Uncertainty values provided in the observed literature values in parentheses, where available.

Beam energy	Axial transition	Observed energy (keV)	Calculated (keV)
4 MeV ²⁵	<100>, 2p-1s	3.80	3.767
16.9 MeV ²⁵	<100>, 2p-1s	58.3 (0.5)	58.48
	<100>, 3d-2p	35.0 (0.5)	35.288
30.5 MeV ²⁵	<100>, 2p-1s	161.6 (2)	163.17
	<100>, 3d-2p	110.4 (1)	118.381
5.2 MeV ²⁶	<110>, 2p-1s	9.38 (0.09)	8.804
9.0 MeV ²⁶	<110>, 2p-1s	24.34 (0.23)	24.481

B. Population dynamics under frozen-phonon scattering

To investigate population dynamics and coherence properties in the following sections, a case study is done for axial channeling in diamond along $\langle 100 \rangle$ at 16.9 MeV electron beam energy using 0.055 Å RMS thermal displacement amplitude. Propagation is carried out up to 2.8 μm crystal thickness with $N_\beta = 30$ phonon configurations. Relevant notation and the numerically extracted ensemble quantities are described next.

The transverse dynamics are analyzed in a tracked Hilbert space decomposed into bound-state manifolds. In an ideal cylindrically symmetric column potential, these manifolds can be indexed by radial and azimuthal quantum numbers, (n, m) [13]. Here we use the corresponding hydrogenic labels as the primary identifiers. Each manifold $M \in \{1s, 2s, 2p, 3d\}$ defines a subspace \mathcal{H}_M spanned by eigenmodes $\{|M, a\rangle\}$ of the transverse Hamiltonian. The $1s$ and $2s$ manifolds are non-degenerate, while $2p$ and $3d$ are twofold degenerate with $\dim \mathcal{H}_M = 2$. The letter a in $|M, a\rangle$ labels a particular basis state of a chosen basis in the degenerate manifold M .

The evolution of the electron under frozen-phonon scattering is captured by projecting the configuration-dependent wavefunction $\psi^{(\beta)}(\mathbf{r}, z)$ onto the manifold basis states:

$$(14) \quad c_{Ma}^{(\beta)}(z) = \langle M, a | \psi^{(\beta)}(z) \rangle.$$

The total population in manifold M for configuration β is (basis-invariant) Born probability:

$$(15) \quad p_M^{(\beta)}(z) = \sum_a |c_{Ma}^{(\beta)}(z)|^2,$$

To quantify population transfer, the incoherent conditional population is defined as:

$$(16) \quad P_M(z|M_0) = \left\langle p_M^{(\beta)}(z) \right\rangle_{\beta},$$

which represents the ensemble-averaged population in manifold M at depth z given an initial excitation in manifold M_0 .

To obtain Fig. 2, the propagation is initialized in a selected normalized transverse eigenmode $\psi(0) = |M_0, a_0\rangle$ of one manifold $M_0 \in \{1s, 2s, 2p, 3d\}$, and projections are tracked into the set of manifolds $M = \{1s, 2s, 2p, 3d\}$ as a function of depth z . Shaded bands indicate one standard deviation, $\pm 1\sigma$, variations across frozen-phonon configurations β at each z . Figure 2 shows that, for all initializations, the population in the originating manifold M_0 decays approximately exponentially under thermal diffuse scattering. More tightly bound states depopulate more rapidly, consistent with increased sensitivity to atomic displacements. Population transfer among the tracked manifolds is distinctly channel dependent. The strongest bound-to-bound coupling occurs between the $1s$ and $2p$, which, when starting from zero-population, display a clear rise due to feeding followed by decay. Coupling between $2p$ and $3d$ is also substantial (panels c–d), whereas $2s$ couples comparatively weakly to the other tracked manifolds.

Although Fig. 2 shows the 16.9 MeV case for brevity, the same qualitative hierarchy of coupling channels persists at 30.5 MeV for the conditions considered, with a generally faster overall decay at higher beam energy.

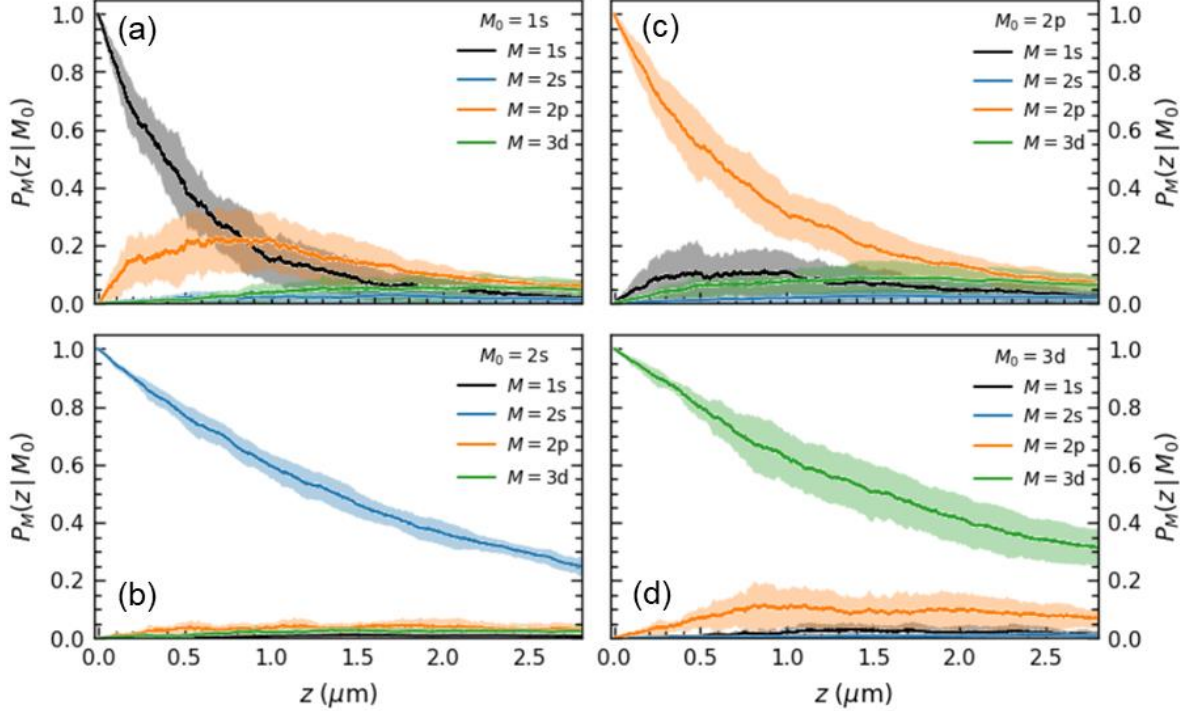


FIG. 2. (a-d) Ensemble-averaged manifold populations $P_M(z|M_0)$ in the tracked bound-state manifolds $\mathcal{M} = \{1s, 2s, 2p, 3d\}$ as a function of depth z , for 16.9 MeV axial channeling in $\langle 100 \rangle$ diamond. Each panel corresponds to propagation initialized in an eigenmode of manifold M_0 , and the curves show the population transferred into each manifold M . Shaded regions indicate $\pm 1\sigma$ variations across frozen-phonon configurations.

C. Coherence within a degenerate manifold

Two coherence questions are considered: (i) intra-manifold coherence, describing phase relations within a degenerate bound-state manifold, and (ii) cross-manifold coherence, describing phase relations between distinct manifolds. Both analyses below use 16.9 MeV channeling in $\langle 100 \rangle$ diamond. The corresponding manifold populations $P_M(z|M_0)$ are shown in Fig. 2.

This section focuses on coherence in the $2p$ manifold, which is the minimal level of state information beyond populations. For each frozen-phonon configuration β , the propagated wavefunction is projected onto a chosen orthonormal basis spanning the $2p$ manifold. An orbital-angular-momentum (OAM) basis $\{|+\rangle, |-\rangle\} \equiv \{|m = +1\rangle, |m = -1\rangle\}$ is chosen and the initial state is prepared as an equal superposition:

$$(17) \quad |\psi^{(\beta)}(0)\rangle = |2p, +x\rangle \equiv \frac{|+\rangle + |-\rangle}{\sqrt{2}},$$

i.e. the $+1$ eigenstate of σ_1 in the $\{|+\rangle, |-\rangle\}$ basis. For each frozen-phonon configuration β , the $2p$ projection amplitudes are collected into the two-vector:

$$(18) \quad \mathbf{c}^{(\beta)}(z) = \left(c_+^{(\beta)}(z), c_-^{(\beta)}(z) \right)^T,$$

$$(19) \quad c_{\pm}^{(\beta)} = \langle \pm | \psi^{(\beta)}(z) \rangle.$$

The corresponding $2p$ manifold population is:

$$(20) \quad p_{2p}^{(\beta)}(z) = \left| c_+^{(\beta)}(z) \right|^2 + \left| c_-^{(\beta)}(z) \right|^2.$$

To separate internal coherence from overall population loss, we normalize the projected state within the manifold:

$$(21) \quad \mathbf{u}^{(\beta)}(z) = \frac{\mathbf{c}^{(\beta)}(z)}{\sqrt{p_{2p}^{(\beta)}(z)}},$$

which is well-defined when $p_{2p}^{(\beta)}(z) > \varepsilon$. Configurations below a chosen threshold value, $p_{2p}^{(\beta)}(z) \leq \varepsilon$, are omitted from the ensemble average at that depth. The ensemble-averaged reduced (trace-1) density matrix within the $2p$ manifold, conditioned on occupying $2p$ at depth z , is then:

$$(22) \quad \bar{\rho}_{2p}(z) = \langle \mathbf{u}^{(\beta)}(z) \mathbf{u}^{(\beta)}(z)^\dagger \rangle_\beta.$$

For each configuration β , the Bloch components are computed from the normalized two-vector as:

$$(23) \quad S_i^{(\beta)}(z) = \mathbf{u}^{(\beta)}(z)^\dagger \sigma_i \mathbf{u}^{(\beta)}(z),$$

where σ_i are the Pauli matrices. In the $\{|+\rangle, |-\rangle\}$ basis this gives:

$$(24) \quad S_1^{(\beta)}(z) = 2\text{Re}\left(c_+^{(\beta)}(z) c_-^{(\beta)}(z)^* \right),$$

$$(25) \quad S_2^{(\beta)}(z) = 2\text{Im}\left(c_+^{(\beta)}(z) c_-^{(\beta)}(z)^* \right),$$

$$(26) \quad S_3^{(\beta)}(z) = \left|c_+^{(\beta)}(z)\right|^2 - \left|c_-^{(\beta)}(z)\right|^2.$$

The $2p$ manifold purity is obtained from:

$$(27) \quad \gamma(z) = \text{Tr}\left[\bar{\rho}_{2p}(z)^2\right],$$

which is basis invariant and $1/2 \leq \gamma(z) \leq 1$. As a basis-dependent metric, the coherence of the ensemble-averaged state is also reported, $0 \leq \kappa(z) \leq 1$, obtained from the normalized $\bar{\rho}_{2p}(z)$ off-diagonal

$$(28) \quad \kappa(z) = 2\left|\bar{\rho}_{2p,+-}(z)\right|.$$

Figure 3(a) shows $\gamma(z)$ together with $\kappa(z)$ for the initially pure superposition ($\gamma(0) = \kappa(0) = 1$). The purity decreases with depth toward the maximally mixed limit ($\gamma \rightarrow 1/2$), while $\kappa(z)$ decays to small values. Figure 3(b) shows the ensemble-averaged Bloch components $\langle S_i(z) \rangle_\beta$. The component aligned with the prepared superposition, $\langle S_1(z) \rangle_\beta$, starts near unity and decays with depth, whereas $\langle S_2(z) \rangle_\beta$ and the population-imbalance component $\langle S_3(z) \rangle_\beta$ remain near zero in the ensemble mean. In addition, the $\pm 1\sigma$ bands of $\langle S_i(z) \rangle_\beta$ show significant configuration-to-configuration dispersion of Bloch trajectories.

These results, taken together, are indicative of stochastic and β -dependent internal-basis rotations within the degenerate manifold. In a fixed basis employed for the analysis, this appears as the relative-phase randomization and rapid statistical mixing within the manifold. The same behavior is expected in any internal basis of a degenerate manifold, since the ensemble of mean-zero, approximately isotropic thermal displacements does not select a preferred axis. The analysis was also performed in a rotated $2p$ basis ($|\pm x\rangle$), preparing an initial state with $\langle S_3(0) \rangle_\beta = 1$. Again, the initially nonzero initial Bloch component decays toward zero and $\gamma(z) \rightarrow 1/2$. Applying the same diagnostics to the degenerate $3d$ manifold (not shown) reveals substantially slower mixing, consistent with its more spatially extended transverse modes and reduced sensitivity to thermal atomic displacements.

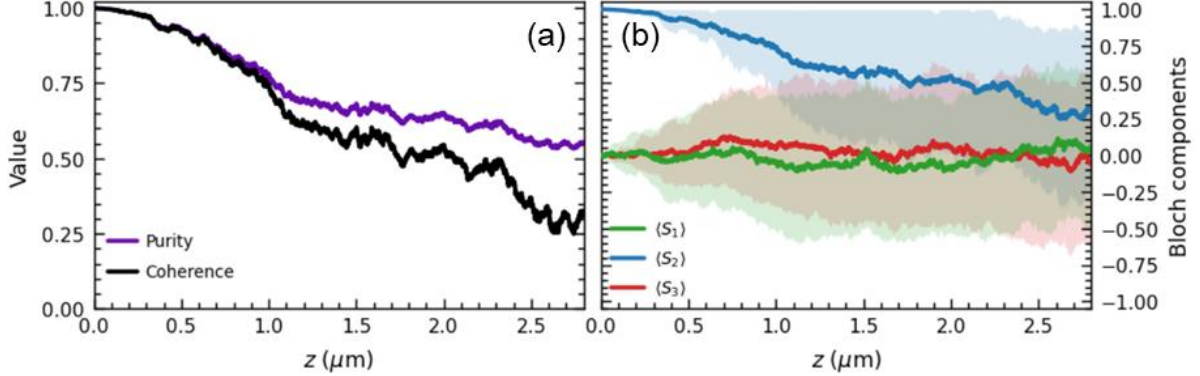


FIG. 3. (a) Ensemble-averaged purity $\gamma(z)$ and ensemble-averaged normalized coherence $\kappa(z)$, in the $M = 2p$ manifold for initial $M_0 = 2p$ excitation starting from an equal superposition of the two OAM basis states $|+\rangle$ and $|-\rangle$. (b) Ensemble-averaged Bloch components $\langle S_i(z) \rangle_\beta$ with shaded $\pm 1\sigma$ bands across configurations β .

D. Cross-manifold coherences

In on-axis channeling radiation experiments the incident beam is typically collimated or weakly convergent, illuminating many atomic columns simultaneously. Among bound states, the initial overlap is therefore dominated by the $m = 0$ manifolds. Population in $|m| > 0$ manifolds, and therefore the radiative channels that involve them, then arises primarily through non-radiative, quasi-elastic thermal diffuse scattering. For 16.9 MeV channeling in $\langle 100 \rangle$ diamond with an initially prepared $1s$ state, this section quantifies the depth-resolved purity of the initially unoccupied $2p$ and $3d$ manifolds and the surviving cross-manifold coherence in the radiative channels $2p \rightarrow 1s$ and $3d \rightarrow 2p$.

To quantify coherence between two manifolds A and B with dimensions $d_A, d_B \in \{1,2\}$, we first collect the per-configuration projection amplitudes as two-vectors, $\mathbf{a}^{(\beta)}(z) \in \mathbb{C}^{d_A}$ and $\mathbf{b}^{(\beta)}(z) \in \mathbb{C}^{d_B}$, in chosen orthonormal bases within each manifold. The associated cross-block matrix is:

$$(29) \quad \mathbf{X}_{AB}^{(\beta)}(z) = \mathbf{a}^{(\beta)}(z) \mathbf{b}^{(\beta)}(z)^\dagger \in \mathbb{C}^{d_A \times d_B}.$$

Using ensemble-averaged cross block, $\langle \mathbf{X}_{AB}(z) \rangle_\beta$, a basis-invariant Frobenius-normalized cross-coherence, $0 \leq C_F^{A,B}(z) \leq 1$, is defined as:

$$(30) \quad C_F^{A,B}(z) = \frac{\|\langle \mathbf{X}_{AB}(z) \rangle_\beta\|_F}{\sqrt{\langle p_A(z) \rangle_\beta \langle p_B(z) \rangle_\beta}},$$

$$(31) \quad p_A^{(\beta)}(z) = \|\mathbf{a}^{(\beta)}(z)\|^2, \quad p_B^{(\beta)}(z) = \|\mathbf{b}^{(\beta)}(z)\|^2.$$

The Frobenius norm, $\|\cdot\|_F$, ensures invariance of $C_F^{A,B}(z)$ under independent unitary basis rotations within manifolds A and B [27]. Numerically, $C_F^{A,B}(z)$ is evaluated only where the denominator exceeds a threshold to avoid instabilities at vanishing populations. In practice, the number of contributing FP configurations remains near maximal ($\sim N_\beta$) across the depth range, indicating that the values are not biased toward a small subset.

Purities in the $2p$ and $3d$ manifolds are evaluated as in the previous section, but here for initialized pure $1s$ eigenmode. Figure 4(a) shows that the conditioned intra-manifold purities of $2p$ and $3d$ remain close to the maximally mixed limit, $\gamma(z) \approx 1/2$, over the full depth range. This indicates that population transferred from $1s$ into these degenerate manifolds does not retain coherence in any fixed intra-manifold basis. The inset in Fig. 4(a) confirms this showing the ensemble-averaged Bloch components in $2p$ remain near zero with large configuration-to-configuration spread. The same behavior is observed for $3d$ (not shown).

Figure 4(a) also reports the Frobenius-normalized cross-coherences for the manifold pairs $(1s, 2p)$ and $(2p, 3d)$ under $1s$ excitation. The cross-coherence remains weakly nonzero with $C_F^{A,B}(z) \sim 0.2$ over the depth range, indicating a residual coherent coupling between the manifolds. Second, Fig. 4(b) shows the (population-unnormalized) real parts of the individual ensemble-averaged cross-block elements $\text{Re} \langle X_{ij}(z) \rangle_\beta$ for the $2p-3d$ block, with i and j indexing the chosen bases in $2p$ and $3d$. Each element exhibits a small, bounded, oscillatory component after ensemble averaging, with frequency set by the transverse eigenenergy differences. The oscillation amplitudes and relative phases drift with depth, reflecting stochastic thermal perturbations.

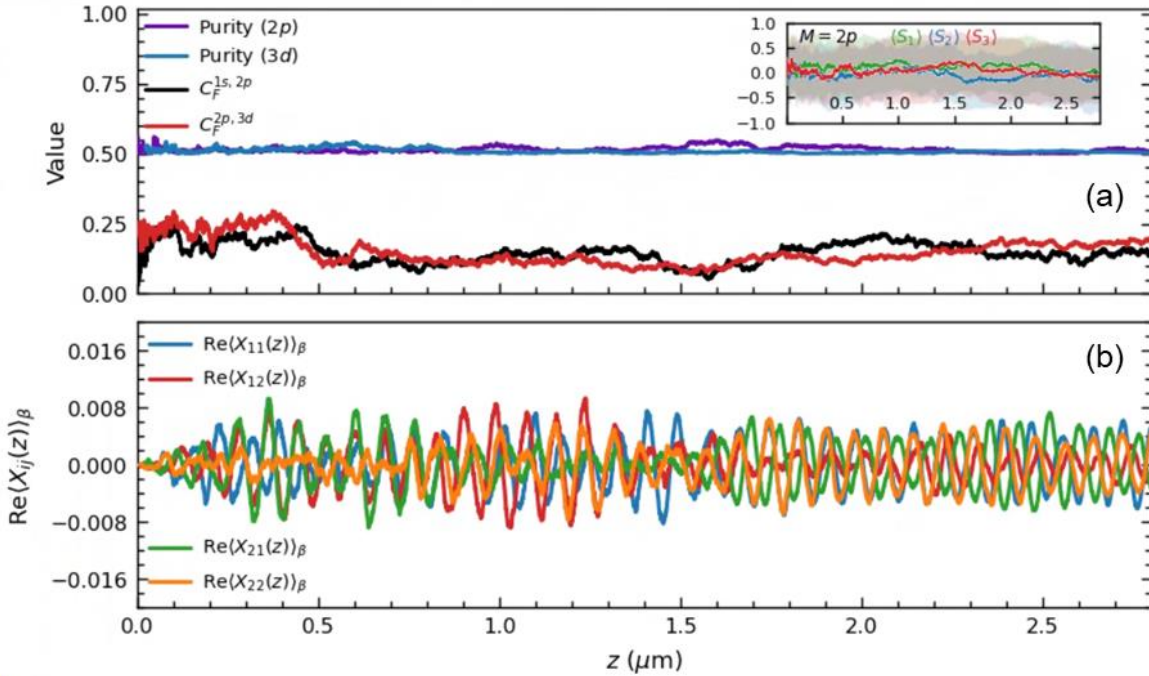


FIG. 4. (a) Intra-manifold purities $\gamma(z)$ for the degenerate $2p$ and $3d$ manifolds, together with Frobenius-normalized cross-coherences $C_F^{A,B}(z)$ for the manifold pairs $(1s, 2p)$ and $(2p, 3d)$, under $1s$ excitation. Inset shows configuration-averaged Bloch components $\langle S_i(z) \rangle_\beta$ within the $2p$ manifold for the same $1s$ -initialized ensemble. (b) Population-unnormlized ensemble-averaged cross-block elements $\text{Re} \langle X_{ij}(z) \rangle_\beta$ for the $2p$ – $3d$ cross block, where i and j index the chosen bases in the $2p$ and $3d$ manifolds, respectively.

III. DISCUSSION

Figure 4(a) shows $\gamma(z) \rightarrow 1/2$ for both $2p$ and $3d$, and $\langle S_i(z) \rangle_\beta \approx 0$, indicating that configuration-dependent rotations within these degenerate subspaces wash out any fixed-basis coherence. The cross-block instead probes whether amplitudes remain correlated within the same frozen-phonon configuration. For a degenerate $2p$ – $3d$ manifold pair, a convenient decomposition to see this is:

$$(32) \quad \mathbf{a}^{(\beta)}(z) = c_A^{(\beta)}(z) U_A^{(\beta)}(z) \mathbf{u},$$

$$(33) \quad \mathbf{b}^{(\beta)}(z) = c_B^{(\beta)}(z) U_B^{(\beta)}(z) \mathbf{v},$$

where $c_A^{(\beta)}(z)$ and $c_B^{(\beta)}(z)$ are scalar pre-factors collecting the overall magnitude and global phase of the manifold projections (e.g., $c_A^{(\beta)} \propto ||\mathbf{a}^{(\beta)}||e^{i\theta_A^{(\beta)}}$), $U_A^{(\beta)}(z)$ and $U_B^{(\beta)}(z)$ are configuration-dependent unitary rotations within them, and \mathbf{u}, \mathbf{v} are fixed reference unit vectors (a gauge choice). Then the cross block factorizes as:

$$(34) \quad \mathbf{X}_{AB}^{(\beta)}(z) = c_A^{(\beta)}(z) c_B^{(\beta)}(z)^* U_A^{(\beta)}(z) \mathbf{u} \mathbf{v}^\dagger U_B^{(\beta)}(z)^\dagger.$$

Random internal rotations $U_A^{(\beta)}$ and $U_B^{(\beta)}$ suppress fixed-basis intra-manifold Bloch vectors after ensemble-averaging, but they need not eliminate $\langle \mathbf{X}_{AB}(z) \rangle_\beta$. The scalar factor $c_A^{(\beta)} c_B^{(\beta)*}$ and the rotated outer-product $U_A^{(\beta)} \mathbf{u} \mathbf{v}^\dagger U_B^{(\beta)\dagger}$ can retain a small, biased mean, since both manifolds are co-populated by the same initially prepared $1s$ -mode scattering. For $1s - 2p$ cross-block, $U_{1s}^{(\beta)} \equiv \mathbf{1}$, and only the $2p$ -side undergoes configuration-dependent internal rotations.

Coherence enters radiation observables through bilinear contractions of transition amplitudes \mathcal{M}_{fm} with the electronic density matrix ρ_{mn}

$$(35) \quad \frac{d^2N}{d\omega d\Omega} \propto \sum_{f,m,n} \rho_{mn}(z) \mathcal{M}_{fm}(\omega, \Omega) \mathcal{M}_{fn}^*(\omega, \Omega).$$

Diagonal elements ρ_{mm} give population-weighted intensities while off-diagonals ρ_{mn} contribute interference terms whenever the measurement does not resolve the “which-state” information [28]. Intra-manifold dephasing in the degenerate subspaces thus controls polarization and azimuthal anisotropy of lines emitted from these manifolds. The residual cross-coherence $\langle \mathbf{X}_{AB} \rangle_\beta$, discussed in the final section, quantifies cross-manifold phase correlation (“optical” coherence). Such high-frequency phase correlations are typically washed out in incoherent photon-yield spectra, but can become relevant under phase-sensitive conditions, for example in externally driven or stimulated channeling radiation schemes.¹⁵ In that regime, thermal decoherence and population kinetics set the coherence lifetime and therefore the achievable control contrast.

IV. CONCLUSIONS

A frozen-phonon multislice framework is introduced for MeV-range channeling dynamics, where the bound-state spectrum is strongly quantized. Beyond transverse-energy extraction, FP propagation provides access to quantities that are typically inaccessible in mean-field treatments. The configuration-resolved bound-state projection amplitude analysis enables evaluation of ensemble-averaged manifold populations, reduced density matrices within degenerate manifolds, and coherence metrics. As a use-case demonstration, 16.9 MeV axial channeling in $\langle 100 \rangle$ diamond is studied. The manifold populations exhibit approximately exponential TDS-driven decay, with more tightly bound states depopulating faster. Population transfer is strongly manifold dependent, with particularly pronounced coupling among $1s \leftrightarrow 2p$ and $2p \leftrightarrow 3d$ under the conditions studied. For an initially pure superposition within the $2p$ manifold, the state evolves from pure toward near-maximally mixed, and the Bloch-vector components indicate configuration-dependent random basis rotations leading to decoherence in a fixed-basis setting. Under $1s$ initial excitation, population transferred into the $2p$ and $3d$ manifolds remains close to maximally mixed, but a small residual cross-manifold coherence persists, and cross-block elements show oscillations after configuration averaging. The wave-propagation approach is particularly well suited to the study of deeply bound, strongly quantized transverse-state dynamics, and it generalizes to arbitrary crystal geometries.

DATA AVAILABILITY

The data are available from the authors upon reasonable request.

References

- [1] J. U. Andersen, E. Bonderup, and R. H. Pantell, *Annu. Rev. Nucl. Part. Sci.* **33**, 453 (1983).
- [2] J. U. Andersen, E. Bonderup, E. Lægsgaard, B. B. Marsh, and A. H. Sørensen, *Nucl. Instrum. Methods* **194**, 209-224 (1982).

[3] S. Datz, R. W. Fearick, H. Park, R. H. Pantell, R. L. Swent, J. O. Kephart, R. K. Klein, and B. L. Berman, *Phys. Lett. A* **96**, 314 (1983).

[4] G. B. Sushko, A. V. Korol, and A. V. Solov'yov, *Phys. Rev. Accel. Beams* **27**, 100703 (2024).

[5] C. K. Gary, A. S. Fisher, R. H. Pantell, J. Harris, and M. A. Piestrup, *Phys. Rev. B* **42**, 7 (1990).

[6] H. Park, J. O. Kephart, R. K. Klein, and R. H. Pantell, M. V. Hynes, B. L. Berman, B. A. Dahling, S. Datz, R. L. Swent, and M. J. Alguard, *Phys. Rev. B* **35**, 13 (1987).

[7] A. I. Akhiezer, N. F. Shul'ga, V. I. Truten', A. A. Grinenko, and V. V. Syshchenko, *Phys. Rep.* **203**, 289 (1991).

[8] E. Bagli, V. Guidi, and V. Maisheev, *Eur. Phys. J. C* **74**, 2996 (2014).

[9] A. A. Savchenko, A. A. Aryshev, M. A. Shevelev, and A. P. Potylitsyn, *Nucl. Instrum. Methods Phys. Res., Sect. A* **1060**, 169007 (2024).

[10] M. Gouanère, D. Sillou, M. Spighel, N. Cue, M. J. Gaillard, R. G. Kirsch, J. C. Poizat, J. Remillieux, B. L. Berman, P. Catillon, L. Roussel, and G. M. Temmer, *Phys. Rev. B* **38**, 4352 (1988).

[11] A. V. Tulupov, *Radiat. Eff.* **56**, 77 (1981).

[12] N. F. Shul'ga, V. V. Syshchenko, A. I. Tarnovsky, and A. Yu. Isupov, *J. Phys.: Conf. Ser.* **732**, 012034 (2016).

[13] N. F. Shul'ga, A. A. Greenenko, and V. I. Truten, *Nucl. Instrum. Methods Phys. Res., Sect. B* **145**, 73 (1998).

[14] V. A. Bazylev and N. K. Zhevago, *Radiat. Eff.* **54**, 41–50 (1981).

[15] A. Friedman, A. Gover, G. Kurizki, S. Ruschin, and A. Yariv, *Rev. Mod. Phys.* **60**, 471 (1988).

[16] K. B. Korotchenko, Y. P. Kunashenko, and S. B. Dabagov, Eur. Phys. J. C **82**, 196 (2022).

[17] R. Fusina, Phys. Rev. B **42**, 7706 (1990).

[18] V. Epp, J. Janz, and M. Zotova, Nucl. Instrum. Methods Phys. Res., Sect. B **436**, 78 (2018).

[19] E. J. Kirkland, *Advanced Computing in Electron Microscopy*, 2nd ed. (Springer, New York, 2010).

[20] R. F. Loane, P. Xu, and J. Silcox, Acta Crystallogr. Sect. A **47**, 267 (1991).

[21] P. M. Zeiger, J. Barthel, L. J. Allen, and J. Rusz, Phys. Rev. B **108**, 094309 (2023).

[22] M. Suzuki, J. Math. Phys. **32**, 400 (1991).

[23] P. A. Doyle and P. S. Turner, Acta Crystallogr. Sect. A **24**, 390 (1968).

[24] M. D. Feit, J. A. Fleck, Jr., and A. Steiger, J. Comput. Phys. **47**, 412 (1982).

[25] R. K. Klein, J. O. Kephart, R. H. Pantell, H. Park, B. L. Berman, R. L. Swent, S. Datz, and R. W. Fearick, Phys. Rev. B **31**, 68 (1985).

[26] H. Genz, L. Groening, P. Hoffmann-Stascheck, A. Richter, M. Höfer, J. Hormes, U. Nething, J. P. F. Sellschop, C. Toepffer, and M. Weber, Phys. Rev. B **53**, 8922 (1996).

[27] T. Baumgratz, M. Cramer, and M. B. Plenio, Phys. Rev. Lett. **113**, 140401 (2014).

[28] L. Mandel and E. Wolf, *Optical Coherence and Quantum Optics* (Cambridge University Press, Cambridge, 1995).